Research paper

Fatigue lifespan of a planetary roller-screw mechanism

Juliette Lepagneul, Loïc Tadrist *, Jean-Michel Sprauel, Jean-Marc Linares

Aix-Marseille Université, CNRS, ISM, Marseille, France

ARTICLE INFO

ABSTRACT

Electro-mechanical actuators including planetary roller screw (PRS) support cyclic loads in aeronautical conditions. PRS multiple thread contacts between screw, rollers and nut allow the mechanism to support large loads. However, aeronautical accreditation requires fine prediction of fatigue lifespan. In this paper, a fatigue design strategy for PRS mechanisms is proposed combining Hertz contact model and a multi-axial fatigue criterion. The method is applied on two examples, one standard and one inverted PRS.

The lifespan of PRS mechanism depends on maximal Dang Van stress. The Hertz sliding angle (Hertz contact main direction/sliding velocity) was introduced to analyze PRS performances. For both examples, the maximum stress at thread contact were located in bulk material but not at the surface. Dang Van stress mainly depended on curvature ratio, Hertz sliding angle and loads. Based on this analysis, Dang Van criterion was implemented to derive the loading domain of infinite lifespan of the mechanism. Critical contact was not always on the roller-screw side.

1. Introduction

In industry, electro-mechanical actuators (EMA) outperform conventional linear hydraulic actuators in terms of maintainability, reliability, and manoeuvrability. For conventional EMA, motor motions are usually reduced and converted by a gearbox and a ball-screw mechanism. The main drawbacks of this technology are high contact pressures, a reduced resistance to dynamical loads and the requirement of an additional reducing element.

Planetary roller-screw (PRS) mechanism was proposed for EMA as an efficient technology combining reduction and conversion of motor motion. The main assets of the PRS mechanism are its load capacity and its reduced weight. PRS high load capacity is permitted thanks to the multiple thread contact points between screw, rollers and nut. However, aeronautical accreditation requires fine prediction of its fatigue lifespan. In this paper, a fatigue design strategy for PRS mechanisms is proposed combining Hertz contact model and a multi-axial fatigue criterion. The method is applied on two examples, one standard and one inverted PRS.

We grounded our fatigue life modeling by classifying PRS literature. Special attention was paid on geometrical models of thread contacts and on load distribution in the mechanism. Both are key elements for fatigue design and were largely discussed in previous works. From this literature review, the geometry and kinematics of the model were described. Then contact and bulk stresses were determined for a set of material properties. Dang Van multi-axial fatigue criterion was implemented. The domain of infinite fatigue life was determined on two examples, a standard and an inverted PRS. Finally, the results are discussed regarding PRS design specifications.

---

* Corresponding author.
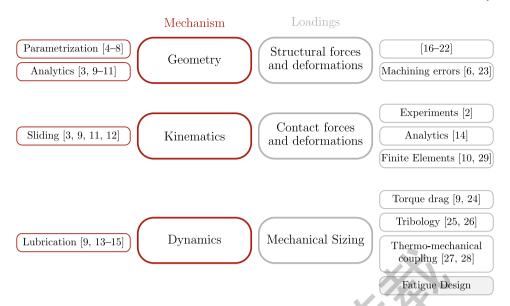 *E-mail address:* loic.tadrist@univ-amu.fr (L. Tadrist).

Fig. 1. Concise view of PRS research domains with main bibliographic references.

2. State-of-the-art

The first planetary roller screw mechanism was patented in 1942, by Strandgren [1]. Since then, little attention has been paid by the scientific community to this mechanism until late 2000. The increase of machine performances renewed interest for this mechanism. Hojjat and Agheli [2] made a study about capabilities and limitations of roller-screw mechanisms. They measured the friction forces thanks to a piezoelectric sensor and showed that slipping was an important aspect of roller-screw contact. They emphasized on the optimization of the thread geometry and number of rollers for displacement accuracy. The same year, Velinsky et al. [3], published a first paper about the efficiency of PRS mechanisms with comparisons with standard ball screw mechanisms.

The proprieties of PRS mechanism were classified in six categories, geometry, kinematics, dynamics, structural forces and deformations, contact forces and local deformations and mechanical sizing (Fig. 1).

2.1. General functioning of the PRS mechanism

The PRS geometry and kinematics strongly influences the mechanism lifespan. They represent basic knowledge of the mechanism and were largely discussed in the literature.

2.1.1. Geometry and parametrization
Following the early works, renewed analysis was done on the parametrization and comprehensive analysis of the PRS mechanism geometry [3–7]. The main geometrical conditions for machining a PRS mechanism were described by Ma et al. [4], instigating concepts such as concentric specification, distribution of rollers, non-interference of threads between roller-screw and roller-nut contacts, etc. A refined parametrization has been proposed recently by Ma et al. [6] to take into account machining errors in PRS mechanisms.

The research of thread contact location were firstly discussed by Velinsky et al. [3]. The contact location were shown not to be in the plane containing the roller and screw axes [5,8]. This work was finally completed by Sandu et al. [9], stating that contact condition was given by the equality of thread normal vectors and implemented numerically with an efficient Newton–Raphson numerical scheme. Those contact conditions are now standard within the PRS community [10].

Contact curvatures of threaded surfaces are influential geometrical parameters since they drive Hertz contact and the capacity of the mechanism to support high loads. Curvatures were first modeled by Ma et al. [4] with an approximate but efficient formula. The exact computation of contact curvatures were done by Jones et al. [11] using tools of differential geometry. This work was further continued by Sandu et al. [12] determining the principal directions of the surface curvatures.

2.1.2. Kinematic and the problem of sliding at thread contacts
The kinematics of roller screw mechanisms was investigated in several works [3,5,12] since sliding at thread contact is a major issue of these mechanisms. The kinematic analysis gives the transformation between the screw rotation velocity ω_0 and the motion of the different pieces in the mechanism. For the fatigue design of a PRS mechanism, sliding is important two folds, (i) it gives the rolling velocity direction at thread contact. (ii) It also gives the amount of rolling-to-sliding ratio ϵ in the mechanism. An approximate ϵ based on kinematic arguments only was proposed by Velinsky et al. [3] and Ma et al. [13]. In a different manner, Sandu et al.

[12] defined the optimal rolling ratio ϵ^*, Eq. (13) for standard PRS mechanisms and Eq. (14) for inverted PRS mechanisms. They emphasized on the fact that ϵ is the result of a complex dynamical process.

2.1.3. Dynamical behavior of a PRS mechanism

The problem of sliding-to-rolling ratio depends on the dynamics of the mechanism, mainly on the lubrication conditions. Indeed the screw, may work for different values of sliding-to-rolling ratio $\epsilon \in [0, \epsilon^*]$ for standard PRS and $\epsilon \in [\epsilon^*, 1]$ for inverted PRS [12]. A detailed dynamical analysis was done by Jones et al. [11] to model the steady state on a PRS mechanism with the sliding-to-rolling ratio as an output. A refined numerical method was proposed by Sandu [14] to model ϵ taking into account lubrication effects. The model prediction was compared to actual measurements. A complete analysis of PRS mechanism dynamical behavior with transient and steady states was carried out by Fu et al. [15].

The numerical computations of ϵ from the different models usually lead to similar values close to ϵ^*, the optimal rolling.

2.2. Load distribution in a PRS mechanism

For the purpose of fatigue design, the second most influential parameter after parametrization and kinematics of the mechanism is the distribution of static loads. The distribution of static loads may be changed by (i) the structural compliance of the mechanism, (ii) the contact compliance and (iii) the machining errors of the mechanism.

2.2.1. Structural deformations

When loaded, the mechanism pieces may deform under the load [16–22]. Analytical and numerical models taking into account structural stiffness of the screw and the roller as well as thread contact stiffness were built. They showed that structural deformations lead to non-linear distribution of loads [19–21]. Deviations from uniform load distribution on contacts are in the order of 20% when roller stiffness is taken into account [17]. This deviation from uniform distribution is even larger when structural compliance is not taken into account. The combination of load distribution by mechanism compliance and the global deformations of the PRS elements both affect the lifespan of a PRS mechanism.

2.2.2. Contacts deformations

PRS mechanism lifespan mainly depends on the deformations at thread contacts. Contact deformations have been studied experimentally by Hojjat and Agheli [2] and contact geometry cleanly described by Sandu [14]. Due to geometrical complexity, sensitivity analysis were performed using finite elements [10,23]. Contact pressures were estimated by Du et al. [24] for fatigue design.

2.2.3. Machining errors

Machining errors were first taken into account for PRS mechanism used for displacement precision [6]. Recently, machining errors were shown to increase the unevenness of the load distribution [24]. This increases the maximum local loads reducing consequently PRS lifespan.

2.3. Sizing of a PRS mechanism

The characterizations of geometry, kinematics, dynamics and load distribution of PRS mechanisms were done in order to size its elements regarding mechanical constraints. These ones include torque drag, tribology, thermo-mechanical coupling and fatigue design.

2.3.1. Power dissipation

A comprehensive analysis of contact lubrication was carried out by Sandu et al. [12]. 90% of the dissipated power are induced from sliding at thread contact. Power dissipation was shown to be insensitive to mechanism geometry but only influenced by lubrication conditions. A friction torque model of the PRS Mechanism in roller jamming was created by Li et al. [25]. This study shows that the wear of the parts hastens in the case of a blocked roller because the friction torque increases considerably.

Experiments were carried out in order to validate the effect of roughness on contact wear [26]. It is shown that wear hastens in dry or badly lubricated conditions. For well lubricated contacts, a small friction coefficient persists. Recently, Xie et al. [27] studied the influence of the speed of rotation, the axial load as well as the surface roughness on the mechanism lifespan. They deduced that a high precision machining is required to get small contact surface roughness. This would improve the lubrication by decreasing the contact area ratio.

2.3.2. Thermo-mechanical coupling

The assembly order of PRS pieces, the magnitude and direction of the load as well as the temperature conditions on the load distribution were analyzed by Ma et al. [28]. They noted that the temperature difference has a strong impact on the load distribution of the mechanism and in particular on the roller-nut contact. This phenomenon generated by the frictional torque on the contact points was studied in more detail by Du et al. [29].
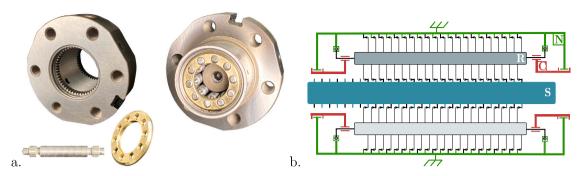
Fig. 2. Standard PRS mechanism. a. Photo of each component (left) and assembled mechanism (right) b. Kinematic diagram of a standard PRS mechanism. The nut (green) is in thread and gear contact with the rollers (gray). The rollers and the screw (blue) are in thread contact. The carriers are in sliding pivot link with the rollers and pivot link with the nut. (For interpretation of the references to color in this figure legend, the reader is referred to the web version of this article.)

2.3.3. Fatigue design

All mechanical constraints presented before apply on the mechanical sizing of a PRS mechanism during functioning, but their effect on the PRS mechanism lifespan remains unknown. This question has been recently addressed by Du et al. [24] where fatigue life is predicted depending on external loads and machining errors thanks to an analysis of maximal contact pressure and a S–N curve.

In this paper, the question of the lifespan of a PRS mechanism in fatigue loading conditions is addressed. With a different approach, a multi-axial loading criterion was applied to determine the fatigue life of a PRS mechanism. Differently from Du et al. [24], maximum stress is computed everywhere in the material including bulk and surface using generalized Hertz model. With this approach, tangential forces are considered.

This analysis of PRS fatigue design starts by parametrizing thread contact geometry and mechanism kinematics.

3. Geometry and kinematics of thread contacts in a PRS mechanism

In this part, PRS mechanism geometrical parametrization is presented. Then, the location of the contact points and their curvatures as well as the definition of the sliding speed are given depending on roller, screw and nut geometries.

3.1. Geometry and parametrization of a PRS mechanism

In brief, a PRS mechanism is an helical link. However its functioning is complex since it involves moving parts (the rollers) between the screw and the nut. Standard and inverted PRS mechanisms are compounded of four types of elements, (i) a nut, (ii) a screw, (iii) several rollers and (iv) two carriers, see Fig. 2a. The PRS kinematic analysis presented hereafter is inspired by the one of Sandu [14].

3.1.1. Components and dimensions

The first element is the internally threaded nut, see Fig. 2a, with a lead $|l| = np$ where n is the number of thread starts and p is the pitch of the thread. The nut is equipped with internal gears at its extremities. The nut is drawn in green color in the kinematic diagram, Fig. 2b.

The second element is the externally threaded screw at the center of mechanism, see Fig. 2a, with a lead $|l| = np$ and pitch p. The screw is drawn in blue color in the kinematic diagram. Measured screw thread profile and thread parametrisation are given in Fig. 3.
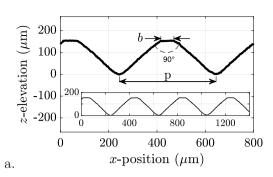
The rollers are small cylinders externally threaded with pitch p and single thread start ($l = p$). Each roller is equipped with gears at both extremities, Fig. 2a. A pair of roller is drawn in light and dark gray in Fig. 2b.

The rollers are maintained in place between the screw and the nut by two carriers, Fig. 2a. Those carriers ensure that the roller axes remain parallel to the nut-screw axes and prevent roller–roller collision. Planetary carriers are drawn in red color in Fig. 2b.

The pitch of the rollers, screw and nut should be equal. Sandu [14] also showed that the lead of the nut and the screw should be the same because of kinematic constraints of non-penetration at thread contacts.

3.1.2. Global kinematics and structural hypothesis

The nut is considered as the reference frame. The rollers have two types of contact with the nut, (i) two gear contacts and (ii) several thread contacts which number depends on the ratio between threaded roller length and pitch. The gear contacts are not necessary to understand the PRS mechanism since they only ensure that all rollers have the same rotation velocity. The thread contact are most important because they transfer the load between the screw and the nut. The thread contacts are modeled by punctual links in the kinematic chain, 2. The roller are also in thread contact with the screw and in sliding pivot with the carriers.
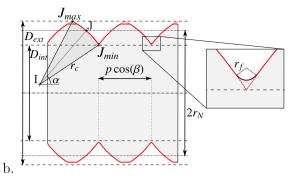
Fig. 3. a. Screw thread cross section obtained by optical microscopy (STIL 3D measuring station). b. Notations and parameters of the threads. I is the center of curvature. J is the point located on the profile and forming an angle $\alpha = 45°$ with the axis of revolution. (J_{max} and J_{min} are boundaries of the mathematical profile).

Table 1
Notations and definition of parameters.

Geometrical parameters		Contact parameters	
p	Pitch	(r_i, θ_i)	Polar coordinates of contact surface i
l	Lead	$\rho_{i,j}$	Principal curvature of surface i, direction j
n	Number of threads	$\overrightarrow{t_{ij}}$	Vector of surface i and principal direction j
r_C	Radius of curvature	ϕ	Angle between $(\overrightarrow{t_{11}}, \overrightarrow{t_{21}})$
D_{ext}, D_{int}	Maximal, minimal diameters	$\overrightarrow{n}$	Contact normal vector
r_N	Nominal radius	$(\overrightarrow{t_1}, \overrightarrow{t_2})$	Tangent vectors (Hertz contact basis)
α	Normal pressure angle		
β	Helice angle		
e	Distance between parallel axis		
γ	Directional convention parameter		
Kinematic parameters		**Mechanical parameters**	
V	Translational velocity of the screw	E	Young Modulus
ω_0	Rotational velocity of the screw	v	Poisson ratio
ϵ	Sliding coefficient	L_t	Fatigue limit in pure torsion
ϵ^*	Sliding coefficient (Maximal rolling)	L_f	Fatigue limit in pure bending
v	Sliding velocity of the contact		
ζ	Hertz sliding angle $(\overrightarrow{v_A}, \overrightarrow{t_1})$		
Contact forces, stress and fatigue parameters			
F	Total loading		
f	Local loading		
f_1, f_2, f_3	Contact loads in the principal basis		
σ_M	Von Mises stress		
τ_{DV}	Dang Van criterion		
z_3	Depth of maximal stress location		

In a standard PRS, the carriers are in pivot link with the nut. Differently in an inverted PRS, the carriers are in pivot link with the screw. For inverted PRS mechanisms, gears are fixed on the screw, instead of the nut for standard ones. Thus screw, rollers and carriers translate relative to the nut for an inverted PRS whereas only the screw translate relative to the nut for a standard PRS. These are the main differences between standard and inverted mechanisms. The model developed in the present paper lies on two main assumptions:

1. The pieces of the PRS mechanism are machined without defects.
2. The solids are rigid except at the thread contact locations where elastic deformations are expected to occur. The loads are supposed to be equi-distributed on the thread contacts.

3.1.3. Cases of reference

The present model is exposed to two examples of reference found in the literature, a standard [4,5,9] and an inverted PRS [8,9]. The geometrical parameters of each example are given in Table 2. The machined pieces are supposed to be made in aeronautical stainless steel of Young modulus $E = 205$ GPa, Poisson ratio $v = 0.3$, the fatigue limit in pure bending of infinite life $L_f = 680$ MPa and the fatigue limit in pure torsion of infinite life $L_t = 426$ MPa [30], see Table 3.

Table 2

Geometrical parameters of the examples of reference. Left: Example 1, standard PRS. Right: Example 2, inverted PRS.

		Example 1: Standard PRS			Example 2: Inverted PRS		
		Screw	Roller	Nut	Screw	Roller	Nut
p	(mm)		2			5	
n		5	1	5	2	1	2
D_{ext}	(mm)	30.9944	10.9070	50.9980	32.4860	17.2954	62.7496
D_{int}	(mm)	29.0056	8.8906	49.0020	27.5140	12.2886	57.7566
α	(°)		45			45	
r_C	(mm)	∞	7.07	∞	∞	10.6064	∞
r_N	(mm)	15	5	25	15	7.5	30.1265
e	(mm)		20			22.5	
γ		−1	1	−1	1	−1	1
β	(°)	6.0664	3.6284	3.6243	6.0566	−6.0566	3.0241
l	(mm)	10	2	10	10	−5	10
ϵ^*			0.3739			0.3326	

Table 3

Material parameters used along the paper for example 1 and 2. Left: Example 1, standard PRS. Right: Example 2, inverted PRS.

		Example 1: Standard PRS	Example 2: Inverted PRS
n_{roller}		10	10
$n_{contact}$		500	500
E	(GPa)	205	205
v		0.3	0.3
L_t	(MPa)	426	426
L_f	(MPa)	680	680

3.2. Contact locations and geometries

We start our analysis by finding contact points between rollers and screw, and rollers and nut. We aim at determining the contact geometries (curvatures and main directions) to use them as inputs for Hertz contact model.

3.2.1. Contact location

The threaded surfaces depend on thread convexity (convex or plane), their mathematical expressions are given by [9],

$$z = \frac{\gamma}{\cos(\beta)} \left(\frac{p\cos(\beta)}{4} + r_c \cos(\alpha) - \sqrt{r_c^2 - r^2} \right) + \frac{\theta l}{2\pi} \qquad \text{convex,}$$

$$z = \frac{\gamma}{\cos(\beta)} \left(\frac{p\cos(\beta)}{4} + (r - r_N)\tan(\alpha) \right) + \frac{\theta l}{2\pi} \qquad \text{plane,} \tag{1}$$

with geometrical parameters defined in Table 1. In most of the configurations, the roller is convex whether the screw and nut are plane. In the following we will consider a convex roller and plane screw and nut. These equations describe the geometry of threaded elements with $\gamma = -1$ for external (screw and roller) top thread and $\gamma = +1$ for external bottom thread. Inversely, for internal thread (nut) $\gamma = +1$ for top thread and $\gamma = -1$ for bottom thread. For each case of study, the contact may occur in two opposite configurations depending on the direction of the load. Fig. 4 exemplifies an applied load in the positive z direction leading to roller-screw contact with top thread for the screw and bottom thread for the roller; and roller-nut contact with top thread for the roller and bottom thread for the nut (Fig. 5 shows a 3D view of the tangent contact). The choice of the force direction is conventional, following examples found in the literature, it has been chosen positive $F > 0$ for example 1 and negative $F < 0$ for example 2. From this surface parametrization, one may define the surface tangent vectors in the frame of reference,

$$\overrightarrow{\omega}(r,\theta) = \begin{pmatrix} r\cos\theta \\ r\sin\theta \\ z(r,\theta) \end{pmatrix} \quad \text{with tangent vectors} \quad \overrightarrow{\omega_r} = \begin{pmatrix} \cos\theta \\ \sin\theta \\ \partial z/\partial r \end{pmatrix} \text{and } \overrightarrow{\omega_\theta} = \begin{pmatrix} -r\sin\theta \\ r\cos\theta \\ l/2\pi \end{pmatrix}, \tag{2}$$

and second order vector derivatives,

$$\overrightarrow{\omega_{rr}} = \begin{pmatrix} 0 \\ 0 \\ \partial^2 z/\partial r^2 \end{pmatrix}, \overrightarrow{\omega_{\theta\theta}} = \begin{pmatrix} -r\cos\theta \\ -r\sin\theta \\ 0 \end{pmatrix} \quad \text{and} \quad \overrightarrow{\omega_{r\theta}} = \overrightarrow{\omega_{\theta r}} = \begin{pmatrix} -\sin\theta \\ \cos\theta \\ 0 \end{pmatrix}. \tag{3}$$
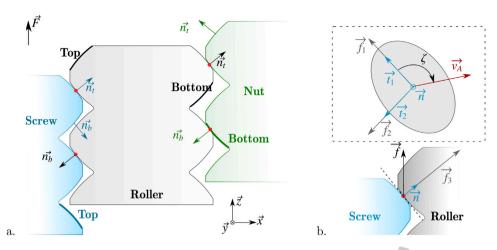
Fig. 4. a. Definition of the orientation of the contact normals. b. Contact frame of reference. Definition of sliding velocity at the contact $\vec{v_A}$ and Hertz sliding angle ζ.
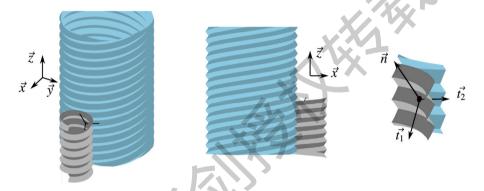

Fig. 5. a. 3D view of the roller-screw contact. b. Normal view of the contact with tangency between the dark gray and dark blue surfaces. c. Zoom on a contact with normal vector $\vec{n}$ and pair of tangent vectors $(\vec{t_1}, \vec{t_2})$ given by Hertz main directions. (For interpretation of the references to color in this figure legend, the reader is referred to the web version of this article.)

From those tangent vectors, one finds the external unit normal vector as

$$\vec{n} = \frac{\overline{\omega_r} \times \overline{\omega_\theta}}{\|\overline{\omega_r} \times \overline{\omega_\theta}\|} \quad \text{leading to} \quad \vec{n} = \frac{1}{\sqrt{\left(\frac{m}{\cos\beta}\right)^2 + \left(\frac{l}{2\pi r}\right)^2 + 1}} \begin{pmatrix} \frac{m}{\cos\beta}\cos\theta - \frac{\gamma l}{2\pi r}\sin\theta \\ \frac{m}{\cos\beta}\sin\theta - \frac{\gamma l}{2\pi r}\cos\theta \\ -\gamma \end{pmatrix}, \tag{4}$$

where m is defined as $m^R = 1/\sqrt{\left(\frac{r_N}{r_1^R \sin\alpha}\right)^2 - 1}$ for the roller and $m^{S,N} = \tan(\alpha)$ for the screw and the nut.

The contact locations are determined by the equality of normal vectors of the two threaded surfaces (tangent surfaces). Fig. 6 shows that the contact location may be characterized in polar coordinates with (r_1^S, θ_1^S) for the screw and (r_2^S, θ_2^S) for roller at the roller-screw contact; and (r_1^N, θ_1^N) for the nut and (r_2^N, θ_1^N) for roller at the roller-nut contact. Radii and angles are obtained by solving the non-linear system of 3 equations given by normal vector equality, for instance for the roller-screw contact, $\vec{n}_{\text{roller}} = -\vec{n}_{\text{screw}}$, for the roller-screw contact. This 3-equation system is reduced to a system of two non-linear equations [9],

$$\left(\frac{m^{S,N}}{\cos\beta_1}\right)^2 + \left(\frac{l_1}{2\pi r_1}\right)^2 - \left(\frac{m^R}{\cos\beta_2}\right)^2 - \left(\frac{l_2}{2\pi r2}\right)^2 = 0, \tag{5}$$

$$\left(\frac{r_1^S \gamma_1 m^{S,N}}{e\cos\beta_1} - \frac{r_2\gamma_2 m^R}{e\cos\beta_2}\right)^2 + \left(\frac{l_1 - l_2}{2\pi e}\right)^2 - \left(\frac{m^{S,N}}{\cos\beta_1}\right)^2 - \left(\frac{l_1}{2\pi r}\right)^2 = 0. \tag{6}$$

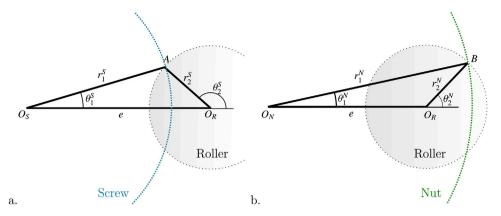This system of equation is solved using Matlab non-linear solver.

Fig. 6. Contacts points between a. screw and roller (A) and b. nut and roller (B). O_S is the center of the screw ; O_N is the center of the nut ; O_R is the center of the roller.

3.2.2. Contact curvatures and directions

Contact curvatures and principal directions are determined using classical tools of surface differential geometry. The Weingarten matrix W, which corresponds to the description of surface curvatures, is made diagonal to find principal curvatures and eigen vectors,

$$W = \frac{1}{\overrightarrow{\omega_r}^2 \overrightarrow{\omega_\theta}^2 - (\overrightarrow{\omega_r}.\overrightarrow{\omega_\theta})^2} \begin{bmatrix} \overrightarrow{\omega_\theta}^2 & \overrightarrow{\omega_r}.\overrightarrow{\omega_\theta} \\ \overrightarrow{\omega_r}.\overrightarrow{\omega_\theta} & \overrightarrow{\omega_r}^2 \end{bmatrix} \cdot \begin{bmatrix} \overrightarrow{\omega_{rr}}.\vec{n} & \overrightarrow{\omega_{r\theta}}.\vec{n} \\ \overrightarrow{\omega_{r\theta}}.\vec{n} & \overrightarrow{\omega_{\theta\theta}}.\vec{n} \end{bmatrix} , \tag{7}$$

where $\overrightarrow{\omega_r}$ and $\overrightarrow{\omega_\theta}$ are the partial derivatives of $\overrightarrow{\omega}$ defined before and $\vec{n}$ the normal vector to the surface.

For instance, considering the screw surface, eigenvalues of Weingarten matrix, $\lambda_{11,12}$ represent the oriented principal curvatures $\rho^S_{11,12} = \gamma \lambda^S_{11,12}$. To make the definition of curvatures unambiguous, the choice $|\rho^S_{11}| \leq |\rho^S_{12}|$ is made. The transfer matrix components $v^S_{11}, v^S_{12}, v^S_{21}, v^S_{22}$ give the principal directions of curvature,

$$\overrightarrow{t^S_{11}} = \frac{v^S_{11}\overrightarrow{\omega_r} + v^S_{12}\overrightarrow{\omega_\theta}}{\left\| v^S_{11}\overrightarrow{\omega_r} + v^S_{12}\overrightarrow{\omega_\theta} \right\|} \quad \text{and} \quad \overrightarrow{t^S_{12}} = \frac{v^S_{21}\overrightarrow{\omega_r} + v^S_{22}\overrightarrow{\omega_\theta}}{\left\| v^S_{21}\overrightarrow{\omega_r} + v^S_{22}\overrightarrow{\omega_\theta} \right\|} . \tag{8}$$

Similarly, $\overrightarrow{t^S_{21}}$ and $\overrightarrow{t^S_{22}}$ are obtained for the roller at the roller-screw contact and $\overrightarrow{t^N_{11}}, \overrightarrow{t^N_{12}}, \overrightarrow{t^N_{21}}$ and $\overrightarrow{t^N_{22}}$ for the roller-nut contact. The angle between the principal directions of the two surfaces in contact is given by

$$\phi = \min \left(\arccos \left(\overrightarrow{t_{11}}.\overrightarrow{t_{21}} \right), \pi - \arccos \left(\overrightarrow{t_{11}}.\overrightarrow{t_{21}} \right) \right) \tag{9}$$

The principal directions $\vec{t_1}$ and $\vec{t_2}$ defining Hertz frame are given by

$$\vec{t_1} = \cos \phi_1 \overrightarrow{t_{11}} + \sin \phi_1 \left(\vec{n} \wedge \overrightarrow{t_{11}} \right) \text{sign} \left((\overrightarrow{t_{11}} \wedge \overrightarrow{t_{21}}).\vec{n} \right) \text{sign}(\overrightarrow{t_{11}}.\overrightarrow{t_{21}}) \quad \text{and} \quad \vec{t_2} = \vec{n} \wedge \vec{t_1} \tag{10}$$

where

$$\phi_1 = \frac{1}{2}\arcsin \left(\frac{|\rho_{22} - \rho_{21}| \sin 2\phi}{\sqrt{\left(\rho_{12} - \rho_{11}\right)^2 + \left(\rho_{22} - \rho_{21}\right)^2 + 2\left|\left(\rho_{12} - \rho_{11}\right)\left(\rho_{22} - \rho_{21}\right)\right| \cos 2\phi}} \right) \tag{11}$$

The values of geometrical parameters of Example 1 and Example 2 are gathered in Table A.4. Those results are compared to those found in literature in Table A.5.

3.2.3. Sliding velocity at the contact

The sliding velocity at the roller-screw contact (Point A) and roller-nut contact (Point B) are given in [9],

$$\overrightarrow{v_A} = \begin{pmatrix} (\epsilon + \lambda - 1)r^S_1 \sin \theta^S_1 \\ e\lambda - (\epsilon + \lambda - 1)r^S_1 \cos \theta^S_1 \\ \chi l^S/2\pi \end{pmatrix} \omega_0 \quad \text{and} \quad \overrightarrow{v_B} = \begin{pmatrix} (\epsilon + \lambda)r^N_1 \sin \theta^N_1 \\ e\lambda - (\epsilon + \lambda)r^N_1 \cos \theta^N_1 \\ (\chi - 1) l^N/2\pi \end{pmatrix} \omega_0 . \tag{12}$$

The set of parameters $(\chi, \Gamma, \epsilon, \lambda)$ are given for the standard PRS as $\chi = 1$, $\Gamma = r_{N,\text{roller}}/r_{N,\text{nut}}$ and $\lambda = -\left(\epsilon\chi + (1 - \epsilon)(1 - \chi)\right)/\Gamma = -\epsilon/\Gamma$. $\epsilon = \omega^{P/N}/\omega^0$ corresponds to the sliding coefficient of the mechanism. It depends on working conditions and varies between 0 (pure sliding) and

$$\epsilon^* = \frac{-\Gamma \left(1 - \Gamma - e \cos \theta^S_1/r^S_1 \right)}{(1 - \Gamma) \left(1 - \Gamma - 2e \cos \theta^S_1/r^S_1 \right) + \left(e/r^S_1\right)^2} \tag{13}$$

which maximizes rolling. Differently, for an inverted PRS, the set of parameters reads $\chi = 0$, $\Gamma = r_{N,\text{roller}}/r_{N,\text{screw}}$ and $\lambda = -(\epsilon \chi + (1 - \epsilon)(1 - \chi))/\Gamma = (\epsilon - 1)/\Gamma$. $\epsilon = \omega^{P/N}/\omega^0$ corresponds to the sliding coefficient of the mechanism. It depends on working conditions and varies between 1 (pure sliding) and

$$\epsilon^* = \frac{1 + \Gamma - (2 + \Gamma) e \cos \theta_1^N / r_1^N + \left(e/r_1^N\right)^2}{(1 + \Gamma)\left(1 + \Gamma - 2e \cos \theta_1^N / r_1^N\right) + \left(e/r_1^N\right)^2} \tag{14}$$

3.3. Forces directions

The total force F is applied on the roller-screw mechanism on the z-axis. At each contact point, F is distributed as $f = F/N_{contact}$ where $N_{contact}$ is the number of contact points between the screw and all the rollers (and similarly for the nut). Firstly, the normal contact force f_3, Fig. 4, projected on the z-axis corresponds to the contact load f, $f_3 = f/\vec{n}.\vec{z}$. The tangent force f_v of projections f_1 and f_2, see 4b, is considered to be proportional to the normal load through a friction coefficient μ,

$$\vec{f_v} = \mu f_3 \frac{\overline{v_A}}{\|\overline{v_A}\|} \quad \text{which projects in} \quad f_1 = \mu f_3 \frac{\overline{v_A}.\overline{t_1}}{\|\overline{v_A}\|} \quad \text{and} \quad f_2 = \mu f_3 \frac{\overline{v_A}.\overline{t_2}}{\|\overline{v_A}\|} \, . \tag{15}$$

The friction coefficient may describe a dry contact but may also be adapted to consider lubricated contact in steady regime.

From this analysis of contact geometry and applied forces (magnitude and directions), we may now determine the surface and bulk stresses from a generalized Hertz model of contact.

4. Contacts loads in the PRS mechanism

In this part, Hertz contact theory is applied to determine the maximum stresses at the contact points.

4.1. Reduction of the contact problem by dimensional analysis

The fatigue contact problem involves 8 physical parameters, the Young's modulus E and Poisson ratio v, main curvatures of Hertz contact ρ_1 and ρ_2, the angle between the sliding velocity and the main direction $\zeta = (\overline{t_1}, \overline{v_A})$, the friction force f_v, the normal load f_3, and the Dang Van criterion limit τ_{DV}. Π theorem reduces the problem to 6 dimensionless numbers. The chosen set of dimensionless parameters is

$$\frac{\rho_1}{\rho_2}, \quad \zeta, \quad \frac{f_v}{f_3}, \quad \frac{f_3(\rho_1 + \rho_2)^2}{E}, \quad \frac{\tau_{\text{DV}}}{E} \quad \text{and} \quad v. \tag{16}$$

Those dimensionless numbers may be gathered in 3 groups, (i) geometrical numbers, ρ_1/ρ_2 and ζ, (ii) material numbers τ_{DV}/E and v and (iii) the loading numbers with the normalized loading $f_3(\rho_1 + \rho_2)^2/E$ and the friction coefficient f_v/f_3.

In the following we will assume that material properties are fixed (τ_{DV}/E and v are treated as constants). The problem thus reduces to only 4 dimensionless numbers, ρ_1/ρ_2, ζ, $f_3(\rho_1 + \rho_2)^2/E$ and f_v/f_3.

4.2. Contact modeling using Hertz theory

The thread contact location are between two non-conforming surfaces where Hertz contact theory applies [14]. The generalized Hertz contact theory is implemented with normal and tangential loads [31,32]. We used, in this paper, a generalized Hertz model already validated and checked [31] which implements equation found in Sackfield's textbook [33].

From the two surface curvatures of surface 1, ρ_{11}, ρ_{12} and the two surface curvatures of surface 2, ρ_{21}, ρ_{22}, and the angle between the directions of the principal axes $\phi = (\overline{t_{11}}, \overline{t_{21}})$, we compute the equivalent curvatures of the Hertz contact ρ_1 and ρ_2 and their directions t_1 and t_2. Applying normal and tangential loads f_3 and f_v, the contact ellipse dimensions, surface stresses and bulk stresses are numerically computed.

4.2.1. Maximal stress scaling

For sanity check of our Hertz model, we consider the evolution of the maximum of Von Mises stress in bulk material on example 1 with normal load only ($f_v = 0$). Von Mises stress is defined as

$$\sigma_{\text{M}} = \frac{1}{\sqrt{2}} \sqrt{(\sigma_{11} - \sigma_{22})^2 + (\sigma_{22} - \sigma_{33})^2 + (\sigma_{33} - \sigma_{11})^2} \tag{17}$$

The evolution of the maximum of Von Mises stress in bulk material $\max(\sigma_{\text{M}})$ as a function of normal force f_3 is plotted in Fig. 7. The loglog plot shows aligned data points correctly fitted with the expected exponent, $\max(\sigma_{\text{M}}) \propto f_3^{1/3}$. This scaling law may be found easily by balancing deformation energy in the volume of the spherical cap by the energy of indentation.
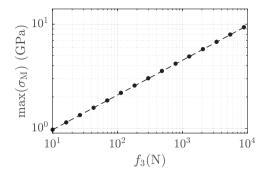
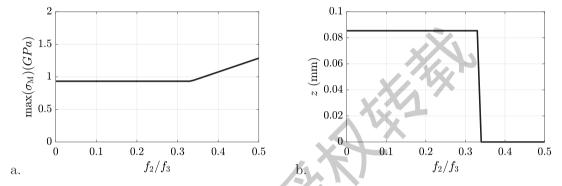**Fig. 7.** Hertz contact scaling of maximal Von Mises Stress $\max(\sigma_M)$ as a function of normal load f_3.

Fig. 8. Standard PRS (example 1) under relative tangential loading f_2/f_3. a. Maximum Von Mises stress σ_M and b. depth of the maximum stress.
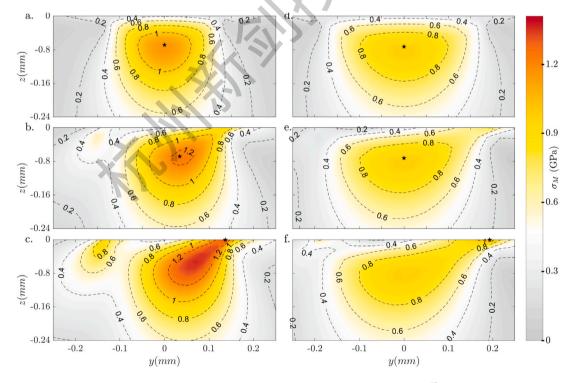

Fig. 9. Color map of Von Mises stress σ_M for example 1 (standard PRS) with normal ($f_3 = 100$ N) and tangential (in $\overline{t_2}$, corresponding here to y-direction) loads. Left column: roller-screw contact (maximal Hertz pressure = 1.87 GPa); Right column: roller-nut contact (maximal Hertz pressure = 1.56 GPa). a and d, $\mu = 0$; b and e, $\mu = 0.25$; c and f, $\mu = 0.4$. ★ corresponds to the depth of the maximum stress z. Sliding coefficient is chosen as $\epsilon = \epsilon^*$, Eq. (13). (For interpretation of the references to color in this figure legend, the reader is referred to the web version of this article.)

4.2.2. Effects of tangential force on the depth of the maximal stress location

We explore the effect of the tangential force on the behavior of the bulk stresses in the case of example 1. To simplify, we consider that the tangential force is in the direction $\vec{t_2}$. For the roller-screw contact, the maximum Von Mises stress $\max(\sigma_M)$ is constant for $f_2 > 0.35 f_3$ and then increases linearly with f_2/f_3, see Fig. 8. The maximum stress is located within the bulk material until the tangential force becomes large, $f_2 > 0.35 f_3$, Fig. 8b, where it comes at the interface.

The color maps of Von Mises stresses in bulk material are plotted in Fig. 9 for the roller-screw contact (a, b, c) and the roller-nut contact (d, e, f). The top graphs, subplot a and d, correspond to $f_2/f_3 = 0$; the middle graphs, subplots b and e, correspond to $f_2/f_3 = 0.25$; and the bottom graphs correspond to $f_2/f_3 = 0.4$. The presence of a tangential force deforms the map of Von Mises stress in the bulk material. The location of the maximal Von Mises stress $\max(\sigma_M)$ initially in the bulk goes at the surface when tangential force is increased. The only difference between left-hand side graphs (roller-screw contact) and right-hand side graphs (roller-nut) is the contact geometry. As the curvatures are smaller in the roller-nut contact, the contact area and the deformed volume is larger leading to lower stresses. In the contrary, as the curvatures between the screw and the roller are larger, it leads to reduced contact area and deformed volume and thus larger stresses.

For a lubricated contact in a PRS mechanism, and even in the case of dry contact, the friction coefficient rarely reaches 0.3. The values of the friction coefficient usually evolve between 0 (perfect lubrication) and 0.1 (dry contact) but our numerical code allows to test a wider range of values to show when the maximal stress moves at the surface. Even under harsh conditions, maximum stress occurs in bulk material.

The stress fields computed using Hertz theory may now be used for fatigue analysis.

5. Fatigue analysis

In the following, fatigue analysis is carried out in bulk and surface considering a multi-axial fatigue criterion, namely the Dang Van criterion [34].

5.1. Dang Van criterion

The Dang Van criterion is based on the local shearing in every direction and hydrostatic pressure. Dang van analysis assumes that in every mesoscopic part of steel, there exists microscopic grains of crystallized steel oriented in every direction. There should be at least one microscopic grain of steel which undergoes shearing in its sliding plane where the crack may initiate. The shear in the direction $\vec{n} = (\sin\psi\cos\phi, \sin\psi\sin\phi, \cos\psi)$, where ϕ and ψ are the azimuth and altitude angles is spherical coordinates, reads

$$\tau = \| \underline{\underline{\sigma}}.\vec{n} - \left(\vec{n}.\underline{\underline{\sigma}}.\vec{n}\right)\vec{n} \|. \tag{18}$$

The hydrostatic pressure does not depend on orientation and reads

$$P = \frac{1}{3}\mathrm{Tr}\left(\underline{\underline{\sigma}}\right) = \frac{1}{3}\left(\sigma_{11} + \sigma_{22} + \sigma_{33}\right). \tag{19}$$

The Dang Van stress is computed from the fatigue limits in pure bending L_f and pure torsion L_t [33],

$$\tau_{DV} = \max_{\{\phi,\psi\}}\left(\tau + 3\left(\frac{L_t}{L_f} - \frac{1}{2}\right)P\right). \tag{20}$$

The infinite life limit is simply given by the Dang Van criterion

$$\tau_{DV} < L_t. \tag{21}$$

5.2. Comparison between roller-screw and roller-nut contacts

Values and depth locations of the maximal Dang Van stress for example 1 (standard PRS) are plotted in Fig. 10 as a function of normal load f_3 and the friction coefficient f_v/f_3 for (a, c) the roller-screw contact and (b, d) the roller-nut contact. For the sake of simplicity, the sliding coefficient is chosen as $\epsilon = \epsilon^*$, Eq. (13).

A solid line separates PRS life domains. On the left is the infinite life domain corresponding to small normal loads. Conversely on the right is the finite life domain corresponding to large normal loads. For roller-screw contact, Fig. 10a and c, this solid line observes a break at $f_2/f_3 = 0.1$ which corresponds to Dang Van stress reaching the interface. For roller-nut contact, Fig. 10b and d, a similar line break occurs at $f_2/f_3 = 0.16$ when Dang Van stress reaches the interface.

Fig. 11a. gathers infinite life domains of roller-screw and roller-nut contacts (Solid line: roller-screw contact. Dashed line: roller-nut contact). The gray area corresponds to infinite life domain of the mechanism when both contacts are considered at the same time. Here, the roller-screw contact is always limiting.

Values and depth location of the maximal Dang Van stress for a inverted PRS (example 2) are plotted in Fig. 12 as a function of normal load f_3 and the friction coefficient f_v/f_3 for (a) the roller-screw contact and (b) the roller-nut contact. Similarly to Fig. 10, the sliding coefficient is chosen as $\epsilon = \epsilon^*$, but now with Eq. (14).

A solid line separates PRS life domains. On the left is the infinite life domain corresponding to small normal loads. Conversely on the right is the finite life domain corresponding to large normal loads. Differently from Example 1, no line break is observed, neither for roller-screw contact nor roller-nut contact.

Fig. 11b. gathers infinite life domains of roller-screw and roller-nut contacts of the inverted PRS, Example 2. For this example, for a classical friction coefficient of 0.05, the roller-screw contact is limiting. However, the two curves cross for a friction coefficient of 0.23 where roller-nut contact is limiting.
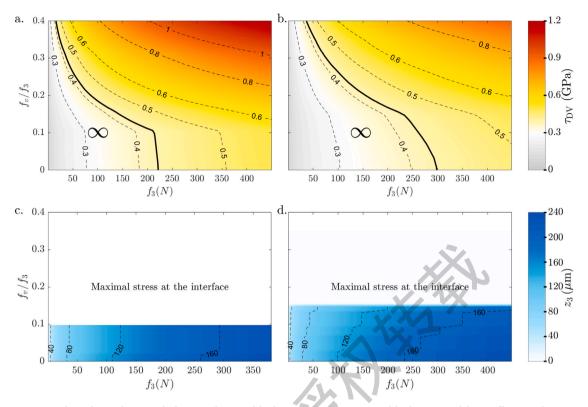
Fig. 10. Fatigue analysis of example 1 (Standard PRS) under normal loading f_3 and relative tangential loading f_v/f_3. Sliding coefficient is chosen as $\epsilon = \epsilon^*$, Eq. (13). Color map of Dang Van stress τ_{DV} for a. roller-screw contact and b. roller-nut contact. Solid line separates infinite PRS life domain (left, corresponding to small normal loads) from finite life domain (right, corresponding to large normal loads). The solid line is given by $\tau_{DV} = L_t$, Eq. (21). Usual friction coefficient are small $f_v/f_3 < 0.1$. Color maps of depth of maximal Dang Van criterion z_{max} for c. roller-screw contact and d. roller-nut contact. (For interpretation of the references to color in this figure legend, the reader is referred to the web version of this article.)
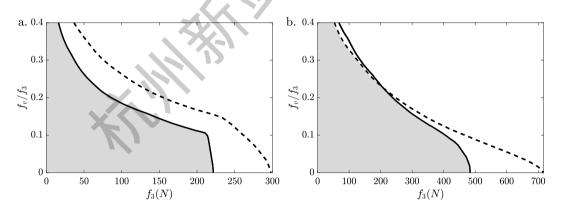

Fig. 11. Mechanism fatigue analysis. a. Standard PRS (example 1) and b. Inverted PRS (example 2) under normal loading f_3 and relative tangential loading f_v/f_3. Sliding coefficient is chosen as $\epsilon = \epsilon^*$. Solid lines correspond to roller-screw contact and dashed lines correspond to roller-nut contact. Gray areas correspond to infinite life domains of the mechanism.

6. Discussion

The behavior of the standard PRS and the inverted PRS are similar regarding fatigue. Theorem Π analysis showed that the problem is ruled by six dimensionless parameters, Eq. (16). In the present study, material parameters (τ_{DV} and ν) were fixed and fatigue maps were plotted as a function of normal load f_3 (which corresponds to the normalized load $f_3(\rho_1 + \rho_2)^2/E$) and friction coefficient f_v/f_3. Thus the change of behavior between the domain boundaries are the effect of the Hertz curvature ratio ρ_1/ρ_2 and the angle between the Hertz main directions and the sliding velocity ζ.
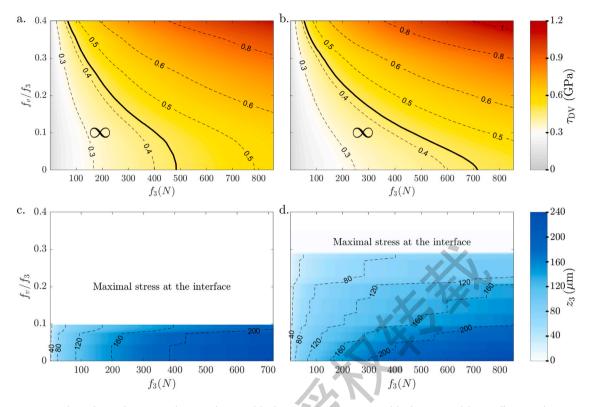
Fig. 12. Fatigue analysis of example 2 (Inverted PRS) under normal loading f_3 and relative tangential loading f_v/f_3. Sliding coefficient is chosen as $\epsilon = \epsilon^*$, Eq. (14). Dang Van stress τ_{DV} for a. roller-screw contact and b. roller-nut contact. Solid line separates infinite PRS life domain (left, corresponding to small normal loads) from finite life domain (right, corresponding to large normal loads). Classically, for steels, friction coefficient is in the order of $f_v/f_3 \simeq 0.1$. Color maps of depth of maximal Dang Van criterion z_{max} for c. roller-screw contact and d. roller-nut contact. (For interpretation of the references to color in this figure legend, the reader is referred to the web version of this article.)

The scaling effect of screw dimensions may be seen directly using the normalized load $f_3(\rho_1 + \rho_2)^2/E$. For instance, considering two similar screws which only differ because the first one has dimensions upscaled by a factor α compared to the other one, it will be able to support a larger load by a coefficient α^2 compared to the other one. This is a direct result of theorem Π. This theorem tells us that if the dimensionless numbers of a problem (here ρ_1/ρ_2, ζ, f_v/f_3, $f_3(\rho_1 + \rho_2)^2/E$, τ_{DV}/E and ν) are kept unchanged then the problem is unchanged. When upscaling the global geometry of the screw, the material properties τ_{DV}/E and ν are not changed as well as the Hertz sliding angle ζ (because it does not involve lengths). The three parameters involving lengths are ρ_1/ρ_2, f_v/f_3, $f_3(\rho_1 + \rho_2)^2/E$, they maybe changed by the upscaling. Clearly, the curvature ratio $(\rho_1/\alpha)/(\rho_2/\alpha) = \rho_1/\rho_2$ is unchanged, and the only other dimensionless parameter that is directly changed by the scaling is the normalized loading $(f_3(\rho_1/\alpha + \rho_2/\alpha)^2)/E$. To keep this number unchanged, the local loading should be upscaled by a factor α^2, $f_3 := \alpha^2 f_3$. This involves that the tangential loading must also be upscaled by a factor α^2 to keep the ratio f_v/f_3 constant. This means that a screw which dimensions are upscaled by a factor α can support loads larger by a coefficient α^2.

In the present examples, the roller-nut contacts have larger curvatures than roller-screw contacts which makes them less limiting regarding the load they can support. However, this is not the only difference between the two contacts, contact curvatures ρ_1/ρ_2 and Hertz sliding angle ζ vary. For example 1 (standard PRS), $\rho_1/\rho_2 = 0.70693$ (respectively 0.75623) for roller-screw contact (respectively roller-nut contact). Since ρ_1/ρ_2 is not close to 1, the contact ellipse is not a circle. For Example 1, the ratio ρ_1/ρ_2 is similar for the roller-screw and the roller-nut contacts. Thus we expect that this dimensionless number does not play much on the different behavior of the two contacts.

Rather, the Hertz sliding angle ζ may have a bigger role as most of the deformations induced by the tangent force occur in the plane containing the sliding velocity vector and the normal. For Example 1 (standard PRS), $\zeta \in [85.38°; 166.93°]$ for the roller-screw contact and it is constant $\zeta = 22.65°$ for the roller-nut contact, see Fig. 15. The variation of ζ corresponds to the small variation of infinite life domain for $\epsilon > 0.3$, Fig. 14b.

The depth of maximal stress is also a critical observable. When the friction coefficient is large enough, both maximal Dang Van stress and Von Mises stress reach the surface as shown on example 1 (Fig. 10d for Dang Van criterion and Fig. 8 for Von Mises stress). The friction coefficient value for which maximal stress occurs at the interface is different for Dang Van criterion ($f_v/f_3 \simeq 0.1$) and Von Mises stress ($f_v/f_3 \simeq 0.35$). This is because Dang Van stress is more sensitive since it considers all the shearing directions whereas Von Mises criterion is independent of direction.
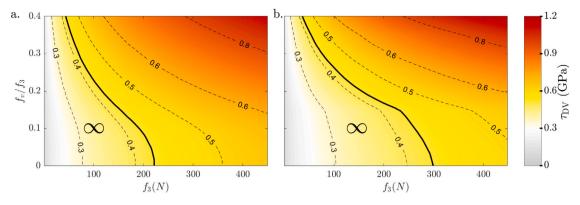
Fig. 13. Fatigue analysis of example 1 (Standard PRS) under normal loading f_3 and relative tangential loading f_v/f_3. Sliding coefficient is chosen as $\epsilon = 0$. Dang Van stress τ_{DV} for a. roller-screw contact and b. roller-nut contact. Solid line separates infinite PRS life domain (left, corresponding to small normal loads) from finite life domain (right, corresponding to large normal loads). Classically, for steels, friction coefficient is in the order of $f_v/f_3 \simeq 0.1$.
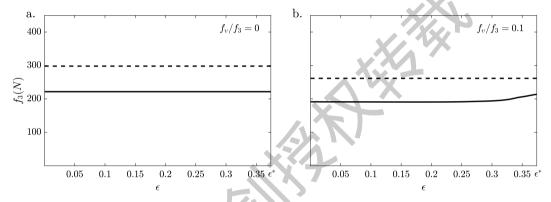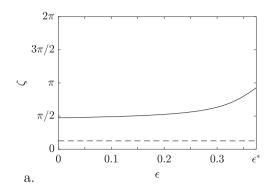

Fig. 14. Standard PRS (example 1) under sliding coefficient and normal loading per contact f_3. Relative tangential loading is chosen as a. $f_v/f_3 = 0$ and b. $f_v/f_3 = 0.1$. Solid line corresponds to roller-screw contact and dashed line corresponds to roller-nut contact.

Particularly for Dang Van stress, when the maximum stress comes at the interface between the two solids, the contact becomes more critical (example 1). This corresponds to the angular point in Fig. 10a and b. For instance in the roller-screw contact, the maximal allowable stress is almost constant before the maximum reaches the interface. However, this line break is not marked for example 2 in Fig. 13. This might be explained by the different configuration of the two examples.

With the dimensional analysis, we can quickly comment the static load ($f_v = 0$) supported at the roller screw contact for example 1 and example 2. The dimensions of example 2 are up-scaled by a factor $\alpha \simeq 7.5/5 = 1.5$ (nominal roller radius). We thus expect that it can withstand load larger by a factor $1.5^2 \simeq 2.25$ which is fairly close to the static load the roller-screw contact can withstand (220 N for example 1 and 480 N for example 2 leading to a ratio of 2.18). The little discrepancy with this rapid up-scaling is mainly due to other factors such as ρ_1/ρ_2 and ζ and relative dimensions between elements which are not conserved between the two examples.

The PRS mechanism functioning is not fully fixed by its kinematics. It depends on the sliding ratio ϵ for which several dynamical models have been proposed [11–13]. In the present paper, the sliding ratio was fixed to the case of maximum rolling $\epsilon^* = 0.3739$. The different models predict values of ϵ extremely close to ϵ^* ($\epsilon_{Jones} = 0.3740$ [11] and $\epsilon_{Ma} = 0.3750$ [13]). To understand the dependency of infinite life domain boundary with ϵ, the case of a pure friction screw (standard PRS, example 1) $\epsilon = 0$ is reported in Fig. 13a for the roller-screw contact and 13b the roller-nut contact. In this case, the fatigue behavior is slightly different with the roller-screw contact being the most critical for $f_v/f_3 < 0.34$ and the roller-nut contact being the most critical for $f_v/f_3 > 0.34$.

The complete dependency of the fatigue results with ϵ was investigated for two given friction coefficients, $f_v/f_3 = 0$ and $f_v/f_3 = 0.1$, which correspond to the limits of no friction and dry contact for steel. Results of maximum allowable loads are plotted in Fig. 14a for $f_v/f_3 = 0$ and 14b for $f_v/f_3 = 0.1$. For frictionless contact, the maximum allowable loads are constant for both roller-screw (solid line) and roller-nut contacts (dashed line). This was expected since if friction coefficient is null, the tangent force is always null independently of the sliding velocity. For $f_v/f_3 = 0.1$, the behavior is different. For small sliding ratio $\epsilon < 0.3$, the maximum allowable load is constant. For larger sliding ratio $\epsilon > 0.3$, the maximum allowable load increases for roller-screw contact. The variations of sliding ratio with the different models encountered in the literature $|(\epsilon - \epsilon^*)/\epsilon^*| < 0.01$ do not change the fatigue results found considering $\epsilon = \epsilon^*$.
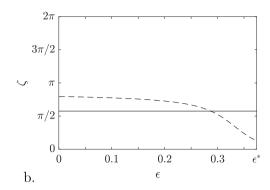
Fig. 15. Hertz sliding angle ζ dependence on sliding coefficient ϵ in a. standard PRS (example 1) and b. inverted PRS (example 2). Solid line corresponds to Roller-Screw contact and dashed line corresponds to Roller-Nut contact.

In Fig. 14b, a decrease in the maximal allowable normal force f_3 with respect to the sliding coefficient ϵ for the roller-nut case is observed for a friction coefficient $f_v/f_3 = 0.1$. This corresponds to a change in the orientation of the sliding speed with the sliding coefficient ϵ, Fig. 15. The Hertz sliding angle ζ increases with sliding ratio ϵ for the roller-screw case whereas no notable change for the roller-nut case is observed. ζ is constant at the roller-nut contact of the standard PRS (15a) or at the roller-screw contact of the inverted PRS (15b) because the sliding speed does not change direction when changing the sliding ratio ϵ (it remains in the $\vec{y}$ direction). For instance, at the Roller-nut contact for a standard PRS, the sliding velocity reads (Eq. (12)b),

$$
\overline{v_B} = \begin{pmatrix} (\epsilon + \lambda) r_1^N \sin \theta_1^N \\ e\lambda - (\epsilon + \lambda) r_1^N \cos \theta_1^N \\ (\chi - 1) l^N / 2\pi \end{pmatrix} \omega_0 = \begin{pmatrix} 0 \\ e\lambda - (\epsilon + \lambda) r_1^N \\ 0 \end{pmatrix} \omega_0
$$

since $\chi = 1$ for a standard PRS and $\theta_1^N \simeq 0$. The direction of this velocity does not change with the sliding ratio ϵ. The same reasoning may be done for an inverted PRS at the roller-screw contact.

A strong assumption made in the present work is the uniform distribution of the load on the threads contacts. Actually, the load does not distribute uniformly on the contacts because of machining defects and mechanism compliance. The first contacts support up to 20% more load than others when compliance is taken into account [17]. Machining defects also create important differences between thread loads [24]. Several models have been proposed to take into account mechanism compliance and may be used to determine the maximum local load f supported by a thread. Machining defects are more difficult to compute using Monte Carlo simulation method. Load dispersion may be considered with a safety factor relative to the uniform distribution load assumption.

An other assumption made in the present paper is that the contact is punctual. We thus considered that the sliding velocity is uniform and at the center of the contact. The non uniformity of the velocity field beneath the contact creates some added shear but this was neglected at the first order in this work. In addition, in some cases where macro sliding is small, Kalker [35] demonstrated that rolling induces micro sliding. This phenomenon was studied in a roller bearing case [36]. This rolling-induced micro sliding creates a compression zone and a traction zone behind the contact where the solid creeps. In this study, the most sensitive contact regarding sliding-induced fatigue is where macro sliding occurs (at the roller-screw contact in a standard PRS; at roller-nut contact in an inverted PRS). Using the proposed model, one can implement a regularized Kalker linear creep theory to consider this effect.

7. Conclusion and perspectives

A fatigue design strategy for PRS mechanisms was proposed. The thread geometry and curvatures are computed using tools of differential geometry. Those geometrical results feed a generalized Hertz contact model which computes the stresses in bulk material and at the surface. From those stresses a multi-axial fatigue criterion is computed to obtain the boundaries of the infinite lifespan domain depending on applied load and friction.

It was shown that the critical thread contact is not always the roller-screw contact but may be the roller-nut contact depending on ρ_1/ρ_2 and Hertz sliding angle ζ. The maximum Dang Van stress is not located at the surface but always in bulk for typical friction coefficient $f_v/f_3 < 0.1$. Dang Van criterion also appears to be m ore sensitive (thus more restrictive) than the Von Mises criterion to define the infinite life domain. The sliding ratio ϵ is an influential parameter but is usually close to the optimal rolling value ϵ^*.

This work determines the maximum loads that a single contact may support as a function of normal load and friction coefficient. This describes well dry contacts with lubricant loss events. However, for lubricated contact, a link between the tangential force of the roller-screw and of the roller-nut contact exists depending on mechanism kinematics. However, the present modeling may be applied directly only by adjusting the macroscopic friction coefficient for each contact.

The infinite-life domain is given in terms of normal and tangential loads. The prediction of this domain only requires the asymptotic values of S–N curves in pure bending L_b and pure torsion L_t. The fatigue lifespan prediction in the finite-life domain (number of cycles) requires the complete knowledge of the two S–N curves in bending and torsion as a function of the number of cycles. Number of cycles in real working conditions are obtained by summing cyclic loads and rotational motion of the rollers.

Table A.4
Complete contact geometry of the two studied examples.

	Example 1: Standard PRS		Example 2: Inverted PRS	
	Screw-roller	Nut-roller	Screw-roller	Nut-roller
r_1 (mm)	15.0357	24.9992	15.0001	29.8417
r_2 (mm)	5.0171	4.9992	7.4999	7.468
θ_1 (deg)	2.3991	$1.1178\ 10^{-4}$	$5.7988\ 10^{-5}$	3.0250
θ_2 (deg)	172.7931	$5.5896\ 10^{-4}$	179.9999	12.1732
ρ_{11} (mm^{-1})	$-2.5484\ 10^{-4}$	$5.6635\ 10^{-5}$	$-2.5664\ 10^{-4}$	$3.3416\ 10^{-5}$
ρ_{12} (mm^{-1})	$4.7545\ 10^{-2}$	$-2.8399\ 10^{-2}$	$4.7659\ 10^{-2}$	$-2.3762\ 10^{-2}$
ρ_{21} (mm^{-1})	0.12897	0.12888	$8.0494\ 10^{-2}$	$8.0379\ 10^{-2}$
ρ_{22} (mm^{-1})	0.1542	0.15429	0.1086	0.10872
$\overrightarrow{t_{11}}$	$\begin{pmatrix} 0.70182 \\ -0.043473 \\ -0.71103 \end{pmatrix}$	$\begin{pmatrix} 0.70428 \\ -0.044566 \\ -0.70853 \end{pmatrix}$	$\begin{pmatrix} -0.69936 \\ -0.072982 \\ -0.71103 \end{pmatrix}$	$\begin{pmatrix} -0.70216 \\ -0.074605 \\ -0.7081 \end{pmatrix}$
$\overrightarrow{t_{12}}$	$\begin{pmatrix} -0.062398 \\ -0.99805 \\ -5.6738\ 10^{-4} \end{pmatrix}$	$\begin{pmatrix} -0.063281 \\ -0.998 \\ -1.2696\ 10^{-4} \end{pmatrix}$	$\begin{pmatrix} 0.10437 \\ -0.99454 \\ -5.7138\ 10^{-4} \end{pmatrix}$	$\begin{pmatrix} 0.10573 \\ -0.99439 \\ -7.5002\ 10^{-5} \end{pmatrix}$
$\overrightarrow{t_{21}}$	$\begin{pmatrix} 0.56731 \\ 0.62814 \\ -0.53253 \end{pmatrix}$	$\begin{pmatrix} -0.48572 \\ -0.6944 \\ -0.53092 \end{pmatrix}$	$\begin{pmatrix} 0.47609 \\ 0.68502 \\ 0.55144 \end{pmatrix}$	$\begin{pmatrix} -0.32281 \\ -0.7705 \\ 0.54966 \end{pmatrix}$
$\overrightarrow{t_{22}}$	$\begin{pmatrix} -0.41785 \\ 0.77681 \\ 0.47114 \end{pmatrix}$	$\begin{pmatrix} 0.51389 \\ -0.71818 \\ 0.46918 \end{pmatrix}$	$\begin{pmatrix} -0.52282 \\ 0.72469 \\ -0.44886 \end{pmatrix}$	$\begin{pmatrix} 0.6661 \\ -0.59753 \\ -0.44641 \end{pmatrix}$
ϕ (deg)	41.4538	86.2713	39.1911	83.969
$\vec{v}$ (at $\epsilon = \epsilon^*$)	$\begin{pmatrix} -0.9870 \\ 0.0623 \\ 1.0000 \end{pmatrix}$	$\begin{pmatrix} -0.9870 \\ 0.0623 \\ 1.0000 \end{pmatrix}$	$\begin{pmatrix} -1.9098\ 10^{-5} \\ 1.8095\ 10^{-4} \\ 0 \end{pmatrix}$	$\begin{pmatrix} -1.9098\ 10^{-5} \\ 1.8095\ 10^{-4} \\ 0 \end{pmatrix}$
ρ_1 (mm^{-1})	0.13686	0.1451	0.08813	0.094432
ρ_2 (mm^{-1})	0.1936	0.10973	0.14836	0.070939
$\overrightarrow{t_1}$	$\begin{pmatrix} 0.69771 \\ 0.18374 \\ -0.69242 \end{pmatrix}$	$\begin{pmatrix} -0.32978 \\ -0.90375 \\ 0.27291 \end{pmatrix}$	$\begin{pmatrix} -0.65522 \\ -0.30475 \\ -0.69124 \end{pmatrix}$	$\begin{pmatrix} -0.23921 \\ -0.91127 \\ -0.33522 \end{pmatrix}$
$\overrightarrow{t_2}$	$\begin{pmatrix} 0.098205 \\ -0.98195 \\ -0.16162 \end{pmatrix}$	$\begin{pmatrix} 0.6255 \\ -0.4257 \\ -0.65386 \end{pmatrix}$	$\begin{pmatrix} 0.26586 \\ -0.94951 \\ 0.1666 \end{pmatrix}$	$\begin{pmatrix} -0.66857 \\ 0.40494 \\ -0.62372 \end{pmatrix}$

Table A.5
Comparison of geometrical analysis for examples 1 and 2 with literature.

	Example 1					
	Current Paper		Sandu [9]		Jones [11]	
	SR	NR	SR	NR	SR	NR
r_1 (mm)	15.0357	24.9992	15.0351	25	15.005	25.0301
r_2 (mm)	5.0171	4.9992	5.0177	5	5.05	5.03
θ_1 (deg)	2.3991	$1.1178\ 10^{-4}$	2.3994	0	2.42	0
θ_2 (deg)	172.7931	$5.5896\ 10^{-4}$	172.7935	0	172.78	0
ρ_{21} (mm^{-1})	0.12897	0.12888	0.1289	–	0.1289	–
ρ_{22} (mm^{-1})	0.1542	0.15429	0.1542	–	0.1542	–
	Example 2					
	Current Paper		Sandu [9]			
	SR	NR	SR	NR		
r_1 (mm)	15.001	29.8417	15	29.8095		
r_2 (mm)	7.4999	7.468	7.5	7.4360		
θ_1 (deg)	$5.7988\ 10^{-5}$	3.0250	0	3.0217		
θ_2 (deg)	179.9999	12.1732	-180	12.1996		
ρ_{21} (mm^{-1})	$8.0494\ 10^{-2}$	$8.0379\ 10^{-2}$	–	–		
ρ_{22} (mm^{-1})	0.1086	0.10872	–	–		

Mechanism compliance and machining defect maybe simply implemented by leveraging on the present theory. As a first approximation, security factor of 50% may be chosen. The code developed in this work may be coupled with a model of load distribution taking into account machining errors and mechanism compliance. This work offers perspectives in the fatigue design of PRS mechanisms depending on screw geometry and materials, with a parametrical sensitivity analysis.

Acknowledgments

Appendix. Data of contact geometries of Example 1 and 2

See Tables A.4 and A.5.

References

[1] C.B. Strandgren, Roulement sur rouleaux pour mouvement hélicoïdal ou circulaire, 1943, FR888281A.
[2] Y. Hojjat, M.M. Agheli, A comprehensive study on capabilities and limitations of roller–screw with emphasis on slip tendency, Mech. Mach. Theory 44 (2009) 1887–1899.
[3] S.A. Velinsky, B. Chu, T.A. Lasky, Kinematics and efficiency analysis of the planetary roller screw mechanism, J. Mech. Des. 131 (2009).
[4] S. Ma, G. Liu, R. Tong, X. Zhang, A new study on the parameter relationships of planetary roller screws, Math. Probl. Eng. 2012 (2012).
[5] M.H. Jones, S.A. Velinsky, Contact kinematics in the roller screw mechanism, J. Mech. Des. 135 (2013).
[6] S. Ma, W. Cai, L. Wu, G. Liu, C. Peng, Modelling of transmission accuracy of a planetary roller screw mechanism considering errors and elastic deformations, Mech. Mach. Theory 134 (2019) 151–168.
[7] X. Fu, G. Liu, S. Ma, R. Tong, T.C. Lim, A comprehensive contact analysis of planetary roller screw mechanism, J. Mech. Des. 139 (2017).
[8] M.E. Fedosovsky, S.A. Aleksanin, R.V. Puctozerov, Use of numerical method for determination of contact points position in roller screw threads, Biosci. Biotechnol. Res. Asia 12 (2015) 721–730.
[9] S. Sandu, N. Biboulet, D. Nelias, F. Abevi, An efficient method for analyzing the roller screw thread geometry, Mech. Mach. Theory 126 (2018) 243–264.
[10] S. Ma, L. Wu, X. Fu, Y. Li, G. Liu, Modelling of static contact with friction of threaded surfaces in a planetary roller screw mechanism, Mech. Mach. Theory 139 (2019) 212–236.
[11] M.H. Jones, S.A. Velinsky, T.A. Lasky, Dynamics of the planetary roller screw mechanism, J. Mech. Robot. 8 (2016).
[12] S. Sandu, N. Biboulet, D. Nelias, F. Abevi, Analytical prediction of the geometry of contact ellipses and kinematics in a roller screw versus experimental results, Mech. Mach. Theory 131 (2019) 115–136.
[13] S. Ma, T. Zhang, G. Liu, R. Tong, X. Fu, Kinematics of planetary roller screw mechanism considering helical directions of screw and roller threads, Math. Probl. Eng. 2015 (2015).
[14] S. Sandu, Developing a Power Dissipation Model for Planetary Roller Screws (Ph.D. thesis), INSA Lyon, 2018.
[15] X. Fu, G. Liu, R. Tong, S. Ma, T.C. Lim, A nonlinear six degrees of freedom dynamic model of planetary roller screw mechanism, Mech. Mach. Theory 119 (2018) 22–36.
[16] F. Abevi, A. Daidie, M. Chaussumier, S. Orieux, Static analysis of an inverted planetary roller screw mechanism, J. Mech. Robot. 8 (2016).
[17] F. Abevi, A. Daidie, M. Chaussumier, M. Sartor, Static load distribution and axial stiffness in a planetary roller screw mechanism, J. Mech. Des. 138 (2016).
[18] F. Abevi, Développement d'un outil d'assistance pour le prédimensionnement d'une vis à rouleaux satellites soumise à des sollicitations complexes (Ph.D. thesis), INSA, Toulouse, 2013.
[19] M.H. Jones, S.A. Velinsky, Stiffness of the roller screw mechanism by the direct method, Mech. Based Des. Struct. Mach. 42 (2014) 17–34.
[20] W. Zhang, G. Liu, R. Tong, S. Ma, Load distribution of planetary roller screw mechanism and its improvement approach, Proc. Inst. Mech. Eng. C 230 (2016) 3304–3318.
[21] W. Zhang, G. Liu, S. Ma, R. Tong, Load distribution over threads of planetary roller screw mechanism with pitch deviation, Proc. Inst. Mech. Eng. C 233 (2019) 4653–4666.
[22] J. Guo, H. Peng, H. Huang, Z. Liu, Y. Huang, W. Ding, Analytical and experimental of planetary roller screw axial stiffness, in: 2017 IEEE International Conference on Mechatronics and Automation, ICMA, IEEE, 2017, pp. 752–757.
[23] L. Zu, Z. Zhang, L. Gao, Design and bearing characteristics of planetary roller screws based on aerospace high-load conditions, Adv. Mech. Eng. 10 (2018) 1687814018811197.
[24] X. Du, B. Chen, Z. Zheng, Investigation on mechanical behavior of planetary roller screw mechanism with the effects of external loads and machining errors, Tribol. Int. 154 (2021) 106689.
[25] L. Li, Y. Fu, S. Zheng, J. Fu, T. Xia, Friction torque analysis of planetary roller screw mechanism in roller jamming, Math. Probl. Eng. 2020 (2020).
[26] G. Auregan, V. Fridrici, P. Kapsa, F. Rodrigues, Experimental simulation of rolling–sliding contact for application to planetary roller screw mechanism, Wear 332 (2015) 1176–1184.
[27] Z. Xie, Q. Xue, J. Wu, L. Gu, L. Wang, B. Song, Mixed-lubrication analysis of planetary roller screw, Tribol. Int. 140 (2019) 105883.
[28] S. Ma, C. Zhang, T. Zhang, G. Liu, S. Liu, Thermo-mechanical coupling–based finite element analysis of the load distribution of planetary roller screw mechanism, Adv. Mech. Eng. 10 (2018) 1687814018775254.
[29] C. Du, G. Liu, G. Qiao, S. Ma, W. Cai, Transient thermal analysis of standard planetary roller screw mechanism based on finite element method, Adv. Mech. Eng. 10 (2018) 1687814018812305.
[30] M. Jabbado, Fatigue polycyclique des structures métalliques: durée de vie sous chargements variables (Ph.D. thesis), Ecole Polytechnique X, 2006.
[31] J. Solle, J.-M. Linares, J.-M. Sprauel, E. Mermoz, Optical measurement for the estimation of contact pressure and stress, CIRP Ann. 61 (2012) 483–486.
[32] A. Sackfield, D. Hills, D. Nowell, Mechanics of Elastic Contacts, Elsevier, 2013.
[33] I.V. Papadopoulos, Long life fatigue under multiaxial loading, Int. J. Fatigue 23 (2001) 839–849.
[34] K.D. Van, Introduction to fatigue analysis in mechanical design by the multiscale approach, in: High-Cycle Metal Fatigue, Springer, 1999, pp. 57–88.
[35] Joost Jacques Kalker, On the rolling contact of two elastic bodies in the presence of dry friction, 1967.
[36] Christophe Bovet, Jean-Marc Linares, Laurent Zamponi, Emmanuel Mermoz, Multibody modeling of non-planar ball bearings, Mech. Ind. 14 (5) (2013) 335–345.